Relationships between Total Water, Condensed Water, and Cloud Fraction in Stratiform Clouds Examined Using Aircraft Data

ROBERT WOOD AND PAUL R. FIELD

Meteorological Research Flight, Farnborough, United Kingdom

(Manuscript received 5 October 1998, in final form 21 July 1999)

ABSTRACT

Relationships among total water, condensed water, and cloud fraction in boundary layer and cold tropospheric stratiform clouds are investigated using a large observational dataset collected by the U.K. Met. Office C-130 aircraft. Values of the above parameters are estimated using horizontal aircraft runs ranging from 40 to 80 km in length. Boundary layer (warm cloud) data were taken from the Atlantic Stratocumulus Transition Experiment (ASTEX) and First International Satellite Cloud Climatology Project (ISCCP) Research Experiment (FIRE). Free tropospheric (cold cloud) data were taken from the European Cloud and Radiation Experiment (EUCREX). In both warm and cold cloud a single reasonably well-defined relationship exists between the cloud fraction and the total water content (vapor + condensate) when normalized with the saturation specific humidity. A relationship exists between the condensed water content and the cloud fraction when appropriately scaled with the saturation specific humidity. Functional forms fitted to the data are used as comparators to test three existing diagnostic cloud fraction parameterization schemes.

1. Introduction

Large-scale numerical weather prediction and climate models are currently unable to resolve atmospheric motions on scales small enough to provide an accurate treatment of cloud formation and dissipation. Even the most high-resolution numerical weather prediction models typically have horizontal grid-box lengths on the order of a few kilometers, whereas the scales most important in cloud formation and dissipation are generally at least one order of magnitude smaller than this. Thus, there is a need to parameterize cloud fraction and condensate amounts, which are affected by subgrid-scale processes.

Many cloud parameterization schemes are based around assumptions of Gaussian or triangular distributions and were originally intended for use in high-resolution cloud models with grid-box lengths less than a kilometer where the only unresolved motions are those on turbulence scales. There is no firm physical evidence to believe that the same assumptions will apply on the grid-box scale of current numerical weather prediction and climate models. Mesoscale motions can occur over a range of scales smaller than the current large-scale model grid length (Atkinson 1981) and currently little is known about these motions and the subsequent affect on the distribution of water vapor.

Early modeling efforts (e.g., Sommeria 1976) made the assumption that a model grid box is either totally saturated or totally unsaturated. It is clear, however, that within a grid box regions of supersaturated *and* subsaturated air can exist and that this results in a partial cloudiness. Sommeria and Deardorff (1977) and Mellor (1977) assume that within a grid box parameters such as total water content and saturation water content are normally distributed around their mean values, a step forward that can be used to derive the cloud fraction within a particular grid box. With similar approaches Le Treut and Li (1988) and Smith (1990) describe the subgrid variation in the difference between the total water content and the saturation water content (saturation specific humidity) using a symmetric triangular distribution. The width of the distribution is controlled using a tunable critical relative humidity parameter, the value of which determines the grid-box mean relative humidity at which cloud starts to form.

Another approach to the prediction of cloud fraction in large-scale numerical models is to use cloud-resolving or cloud ensemble models under a wide range of conditions and identify resulting relationships between the cloud fraction and parameters such as cloud liquid water and relative humidity. If such relationships are relatively well defined over a wide enough range of initialization conditions, then cloud ensemble model data can be used to derive ''semiempirical'' parameter-

Corresponding author address: Dr. Paul R. Field, Meteorological Research Flight, Building Y46, DERA, Farnborough, Hampshire GU14 6TD, United Kingdom.
E-mail: prfield@meto.gov.uk

izations for cloud fraction. From such simulations, parameterizations for cloud fraction can be obtained that depend upon mean cloud liquid water in addition to relative humidity and saturation specific humidity (e.g., Xu and Randall 1996). Parameterizations of this type are therefore only applicable in large-scale numerical models that carry a prognostic liquid water variable.

The possibility of experimentally validating cloud fraction parameterizations for use in large-scale numerical models has not yet been fully explored. Ek and Mahrt (1991) used a limited number of aircraft measurements from the Hydrological and Atmospheric Pilot Experiment (André et al. 1988) and observed a reasonably well-defined relationship between the cloud fraction and the total water content (q_t) normalized with the saturation specific water content (q_s) at the boundary layer top on 10 days. The cloud fraction increased from zero for $q_t/q_s \approx 0.9$ to around 0.8 for $q_t/q_s \approx 1.1$. A relatively large degree of error is attributed to the q_t/q_s measurements by the authors. This error probably arises from the fact that q_t/q_s was estimated from below-cloud aircraft runs using the assumption of well-mixed dry adiabatic conditions between the aircraft height and the boundary layer top.

The purpose of this paper is threefold. The primary aim is to investigate relationships among approximate grid-box scale (≈60 km) means of total specific humidity, cloud condensed water content, and the cloud fraction using aircraft data in the boundary layer and in the free troposphere. The second aim is to examine the cloud fraction parameterization schemes of Slingo (1980), Smith (1990), and Xu and Randall (1996) using the aircraft data. The Tiedtke (1993) scheme was not examined due to the prognostic nature of the scheme. The Sundqvist scheme (Sundqvist et al. 1989) was not examined because values for constants in the cloud fraction equation were not explicitly given in the work. In addition, a numerical fit to the observational data is presented and compared to the results of the three parameterizations. Finally, the third aim of this paper is to make available in situ aircraft measurements of cloud fraction and atmospheric water to enable other workers to assess other cloud fraction schemes.

Section 2 describes the experimental procedure, instrumentation, and analytical methods used. In section 3 observational data are presented and possible relationships between the measured parameters are discussed. Section 4 begins with a brief description of the cloud parameterizations of Slingo (1980), Smith (1990), and Xu and Randall (1996) and proceeds to examine them using the aircraft data. The paper concludes with a brief discussion and possible inferences that can be drawn in the light of the findings.

2. Experimental details and instrumentation

a. Observational data used

Observational data were obtained using the Meteorological Research Flight C-130 aircraft, which has been involved in international collaborative experiments to investigate clouds in the boundary layer and the free troposphere. The data in this study are all taken from constant-altitude runs ranging from 30 to 100 km in length, with approximately 80% of the runs being 50–70 km in length (run lengths are given in appendix B).

The boundary layer data are taken from the Atlantic Stratocumulus Transition Experiment (ASTEX; Albrecht et al. 1995) and the First International Satellite Cloud Climatology Project (ISCCP) Regional Experiment (FIRE; Albrecht et al. 1988) field campaigns. The ASTEX observational campaign was located in the Azores region of the North Atlantic during June 1992, while FIRE observations were made in the stratocumulus region off the southern Californian coast during June–July 1987. ASTEX synoptic conditions were characterized by a high pressure system often with the presence of a strong subsidence inversion at a height of 1–2 km. Cloud types encountered ranged from reasonably thick stratocumulus to trade wind cumulus fields and all condensed water was in the liquid form. In many cases the stratocumulus layer was decoupled from the surface, which allowed a triggering of cumulus cloud patches in the substratocumulus layer at the top of a well-mixed turbulent layer around 500–800 m above the sea surface. Such cumulus clouds often penetrated the stratocumulus layer above maintaining vertical moisture transport from the sea surface to the stratocumulus layer and causing local thickening (Martin et al. 1995). In contrast the FIRE conditions measured by the aircraft were characterized by a much shallower and well-mixed boundary layer (typically less than 1 km deep) in most cases capped with relatively homogeneous stratocumulus cloud. On only one flight from the FIRE dataset used in this study was the boundary layer observed to become decoupled, allowing the formation of cumulus clouds beneath the stratocumulus cloud base.

The free tropospheric data are taken from the European Cloud and Radiation Experiment (EUCREX) field campaign, which was located in Scotland during September–October 1993. Synoptic conditions were characterized by midlatitude cyclonic systems that transferred moisture throughout the troposphere. Cirrus and altostratus clouds were encountered varying from thin, broken, and multilayered structures to thick frontal cloud. Very little liquid water was observed during the flights; only 5% of the EUCREX runs examined in this study contained more than 50% of the condensate in the liquid phase. A summary of all the flights analyzed is given in Table 1. For the purposes of this study, clouds measured in the boundary layer will generally be referred to as warm clouds; those measured in the free troposphere at heights above the freezing level will generally be referred to as cold clouds.

b. Instrumentation and data analysis

A range of instrumentation is used in the analysis. Total water content (q_t = vapor + condensate) is mea-

TABLE 1. Summary of C-130 flights analyzed.

Campaign	No. of flights	No. of runs	Dominant cloud type
FIRE	8	103	Stratocumulus
ASTEX	13	198	Stratocumulus with underlying cumulus
EUCREX	10	54	Frontal cirrus

sured using a Lyman-α hygrometer system referenced to out-of-cloud data from a General Eastern 1011B dewpoint–frost point hygrometer. All condensate mass is initially evaporated by means of two honeycomb heating elements before passing the Lyman-α beam. The probe has been shown to have a very short response time, and data are logged at 64 Hz. The absolute accuracy of the total water content measured with the probe is estimated to be approximately 0.3 g kg^{-1} for the boundary layer data ($q_t \sim$ 6–12 g kg^{-1}) and 0.05 g kg^{-1} for the free tropospheric data ($q_t \sim$ 0.6–2.5 g kg^{-1}). Due to the resolution of the probe it was decided to use only data with run-averaged total water contents greater than 0.6 g kg^{-1}. Further details of the probe are found in Nicholls et al. (1990).

Liquid water content (q_l) was measured using a Johnson–Williams hot-wire probe (Ouldridge 1982). Further details pertaining to the operation of the probe on the Meteorological Research Flight C-130 aircraft can be found in Moss et al. (1993). Data from the probe are logged at 4 Hz, although the estimated time response of the instrument is only around 1 Hz and possibly slower in high liquid water contents. The probe collection efficiency begins to decrease for droplets with radii greater than around 15 μm, falling to around 50% for 250-μm droplets. For the range of droplet sizes encountered in the boundary layer clouds in this study, it has been estimated that the Johnson–Williams probe recovers 90%–100% of the liquid water present and that the liquid water content calibration error is approximately 10%–20%.

Measurement of the ice water content was made with the Lyman-α hygrometer total water probe. Details of the method used for data reduction are presented in appendix A. The accuracy of the ice water content measurements is estimated to be $\pm$0.02 g kg^{-1}.

Temperature was measured using a Rosemount deiced total temperature sensor. Temperature data were corrected for dynamic heating effects using a recovery factor (Harmer et al. 1994). Data from the deiced temperature probe are logged at 32 Hz. The absolute accuracy of the corrected temperature data is estimated to be approximately 0.5 K (Stickney et al. 1994).

The formulas used for the calculation of saturation specific humidity over water and ice are those used by the World Meteorological Organization (e.g., Smith et al. 1990). The error in the derived saturation specific humidity resulting from an instrument error of 0.5 K in temperature rises from around 3% (0.3 g kg^{-1}) in the boundary layer to around 5% (0.02 g kg^{-1}) for the highest aircraft runs (approximately 8000 m) used in this study.

Condensation of vapor to either ice or water produces latent heating and a consequential increase in air temperature. The actual air temperature will therefore be greater than the air temperature prior to condensation, which is known as the liquid water temperature, T_L. In large-scale models the liquid water temperature is a basic variable and we have decided to make use of T_L in presenting the observations. The equation for T_L used in this study is given below (e.g., Smith 1990):

$$T_L = T - (L_w/c_p)q_l - ([L_w + L_i]/c_p)q_i, \qquad (1)$$

where L_w is the latent heat of condensation (vapor $\leftrightarrow$ liquid), L_i is the latent heat of fusion (liquid $\leftrightarrow$ solid), c_p is heat capacity of air at constant pressure, q_l is the liquid water content, q_i is the ice water content, and T is the measured air temperature. In cloud-free air T and T_L are clearly identical. In the clouds observed in this study, the difference between T and T_L is typically smaller than 1 K, but can in cases of high-condensate content be as high as 2 K. A 1 K increase in temperature causes an increase of approximately 0.5 g kg^{-1} in the saturation specific humidity in the boundary layer. In this study, all saturated specific humidities are calculated using T_L.

c. Measurement of cloud fraction

A general problem arising with all cloud fraction measurements, whether they are taken from aircraft, satellites, celiometers, or the human eye, is that for each method of observation a different definition of cloud fraction is used. The meteorological observer uses the term *cloud amount*, which is ''the amount of sky estimated to be covered by a specified cloud type (partial cloud amount) or by all cloud types (total cloud amount)'' (WMO 1996). This measurement differs somewhat from the cloud fraction measurement made by other instruments. For example, a ceilometer defines cloud fraction as the fraction of time for which cloud base can be determined. In this study we define cloud fraction as the fraction of the time (distance) spent in cloud for a given horizontal aircraft run.

Implicit in this analysis is the assumption that data obtained from a single aircraft run are representative of the conditions throughout a two-dimensional area equal to the square of the run length. The extent to which this assumption is true is difficult to assess without prior knowledge of the form of the distribution of cloud throughout the measurement region.

Determination of the presence or absence of cloud in this study was carried out at 1 Hz (equivalent to a measurement averaged over 100 m along the aircraft track) for each aircraft run using cloud droplet concentrations from a forward scattering spectrometer probe (FSSP). A threshold droplet concentration is required to distinguish between cloudy and cloud-free regions. In cloud-

free air the FSSP concentration is generally nonzero due to the presence of large aerosol particles. The concentration of large aerosol particles in clear air is always at least one and often more than two orders of magnitude lower than the concentration of water droplets observed in the ASTEX and FIRE clouds in this study. Large aerosol concentrations were of the order 0.3–2.0 cm^{-3}, whereas cloud droplet concentrations were of the order 50–200 cm^{-3}. Thus, by using a threshold concentration of a few drops per cubic centimeter the presence of clouds can be determined. In this study the results were obtained using a threshold value of 5 cm^{-3}.

The sensitivity of the derived cloud fraction upon the threshold droplet concentration was examined by varying the threshold from 2.5 to 7.5 cm^{-3} for each run. The greatest sensitivity to the change in threshold droplet concentration usually occurred for cloud fractions in the range 0.3–0.7 where the aircraft may be passing into and out of cloud many times during a run. The sensitivity in the cloud fraction to the change in threshold was on occasion as large as 0.3, but for the majority of the cases was less than 0.1. In cases where the cloud fraction is less than around 0.3 or greater than around 0.7 the sensitivity to changes in the threshold liquid water content was significantly reduced.

Cloud fraction for cold clouds was determined in a similar manner to that for boundary layer clouds. A 2D-C optical array probe was used to determine the presence or absence of cold cloud. Qualitatively, time series of particle concentration from the 2D-C and FSSP probes have a similar appearance in cold clouds, but given that the 2D-C has a much larger sample volume and that concentration problems have been encountered when using the FSSP probe in clouds consisting predominantly of ice (Gardiner and Hallett 1985) it was decided that the 2D-C probe was more useful for accurate cloud fraction measurement in cold cloud. A particle concentration threshold of 10 L^{-1} was chosen. The sensitivity of the cloud fraction measurements to changes in the threshold concentration (from 5 to 15 L^{-1}) was investigated. As with the boundary layer cloud fraction measurements using the FSSP the sensitivity was found to be greatest for partially cloudy runs (cloud fraction range 0.3–0.8), where sensitivities of 0.1–0.2 were observed. Again, the sensitivity was smaller outside this range.

3. Observational results

From each straight and level aircraft run a mean quantity was obtained for each parameter. Analyzing the data to examine the variability of a particular parameter along a given aircraft run proved to be difficult because the probability density functions (PDFs) thus derived were generally complex and often exhibited bimodality and large values of skewness. Only a small fraction of the runs had associated PDFs that one might term Gaussian.

Examples of such non-Gaussian PDFs are shown in Fig. 1 adjacent to profiles of total water content, liquid water content, and temperature. Each PDF is constructed from total water content data from a single run either below, in, or above stratocumulus cloud capping a well-mixed boundary layer. The position of the PDF on the page corresponds to the approximate location in the boundary layer shown in the adjacent profiles. For example, the uppermost PDF is taken from a run just above the inversion marking the top of the stratocumulus layer, the next three are from runs in the cloud layer, and the bottom two are from runs below cloud. Although the boundary layer is well mixed [see deRoode and Duynkerke (1997) for an extensive analysis of this case] the PDFs exhibit some complexity, with those in cloud being bimodal. This could be a result of cloud-top cooling entraining relatively dry air into a field of more moist air. The width of the distributions follows no clear trend with height.

Figure 2 is identical in form to Fig. 1, but in this case the cloud and subcloud layer are decoupled from a well-mixed more moist surface mixed layer. Cumulus clouds are observed (550–950 m) to form at the top of the surface layer below the main stratocumulus deck (1600–1900 m). The corresponding PDFs are complex. The lowest run is through the well-mixed surface layer and the corresponding PDF could be described as Gaussian in form. Above the surface layer a variety of different forms exist with bimodal distributions (e.g., at 677 and 1445 m) and strongly skewed distributions (e.g., at 1076 m). These distributions highlight the complex interactions between different levels within the boundary layer. It is difficult to represent these distributions satisfactorily with simple functions for use in a subgrid parameterization scheme. In the following figures data from the three experiments are plotted on the same axes. ASTEX data are denoted by open triangles, FIRE data by plus signs, and EUCREX data by filled circles. Each point represents a single, straight, and level run. The large difference in ambient temperature between the EUCREX and ASTEX/FIRE experiments resulted in a wide range of total water contents. To allow comparison of the relationships among the total water content, the condensed water content, and the cloud fraction, a water content scaling variable is required. Smith's (1990) parameterization scheme uses the mean saturation specific humidity $\overline{q_s}$ as a scaling variable, and so it was considered a suitable choice for use in this analysis. For temperatures below 273.15 K, the freezing point of water, the question arises as to whether the saturation specific humidity scaling variable is that taken with respect to ice or to water. In this study we use a weighted mean $\overline{q_{s(l,i)}}$ of the saturation specific humidity with respect to liquid water $\overline{q_{s(l)}}$ and that with respect to ice $\overline{q_{s(i)}}$, with the weighting of each proportional to the liquid water $\overline{q_l}$ and ice $\overline{q_i}$ in the cloud, that is,

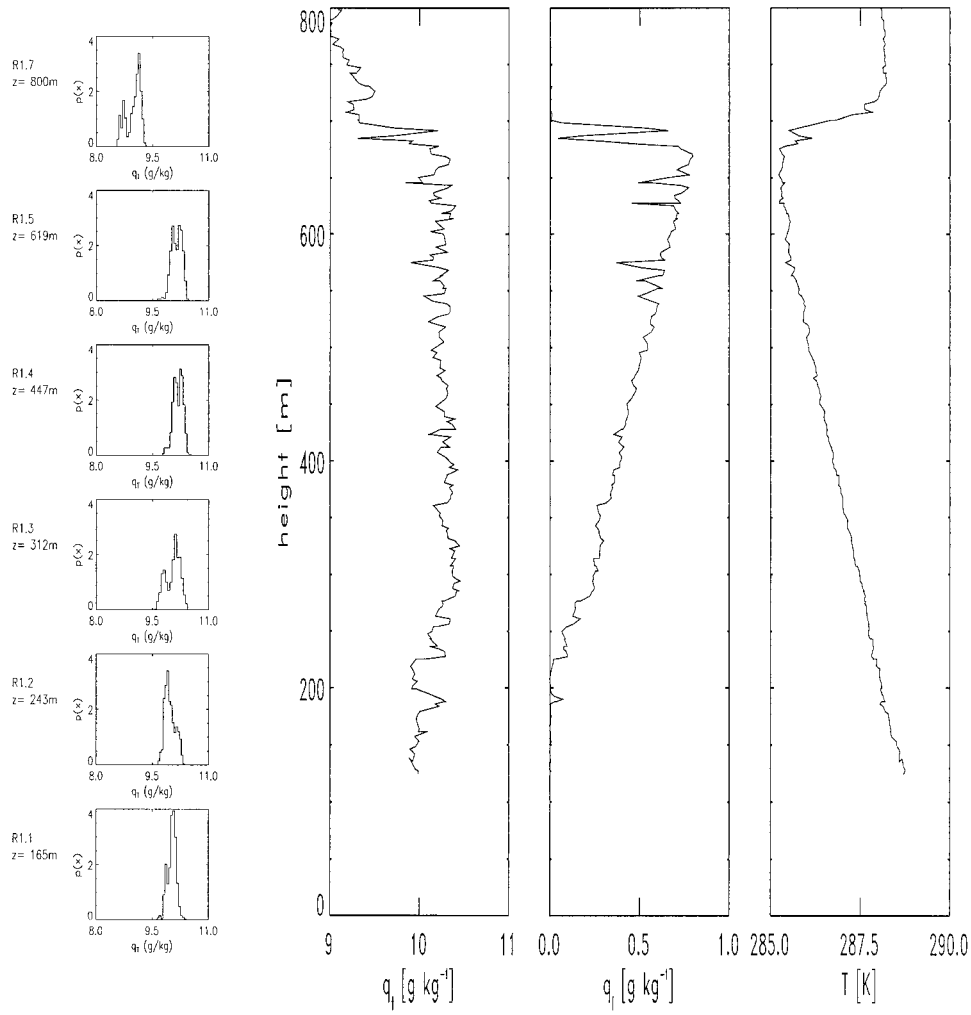

FIG. 1. Distributions of total water from a stack of six horizontal runs through a well-mixed boundary layer with a layer of 8/8 stratocumulus during ASTEX (flight A209), together with the total water, liquid water, and temperature profile.

$$\overline{q}_{s(l,i)} = \frac{\overline{q}_l \overline{q}_{s(l)} + \overline{q}_i \overline{q}_{s(i)}}{\overline{q}_l + \overline{q}_i}. \tag{2}$$

Figure 3 shows the cloud fraction C as a function of the run-mean total water content $\overline{q}_t$ normalized by the run-mean saturation specific humidity $\overline{q}_{s(l,i)}$ (for $\overline{q}_t > 0.6$ g kg^{-1}). Data from the total water content device were unavailable during FIRE and so the total water content in this case is calculated from the sum of the water vapor from the 1011B General Eastern dewpoint hygrometer and the liquid water from the Johnson–Williams probe. The error in $\overline{q}_t/\overline{q}_{s(l,i)}$ is estimated knowing the instrumental errors in temperature and total water content (section 2), and although this error does vary from run to run, it is approximately 0.03–0.05 for the ASTEX data and 0.06–0.08 for the EUCREX data as denoted in the inset in Fig. 3. For the FIRE data the error in $\overline{q}_t/\overline{q}_{s(l,i)}$ is estimated to be 0.04–0.06, which is greater than the error for the ASTEX data as a result of the inaccuracy incurred from the combination of the liquid and vapor content for these data.

The results show that there is an increase in cloud fraction from cloud free ($C = 0$) to fully cloudy ($C = 1$) as $\overline{q}_t/\overline{q}_{s(l,i)}$ increases from 0.80–0.85 to 1.00–1.05. It is interesting that although there is considerable scatter in the data, which is due to the combination of atmospheric variablility and the error in $\overline{q}_t/\overline{q}_{s(l,i)}$, the same broad relationship is found for both warm and cold cloud.

The data are fitted fairly well by a hyperbolic tangent function:

$$C = \frac{1}{2}\{1 + \tanh[A(\overline{q}_t/\overline{q}_{s(l,i)} - B)]\}, \tag{3}$$

which is shown as the thin dotted line in Fig. 3 with the constants $A = 17.0$ and $B = 0.95$ representing the best fit to the data from the three experiments. This

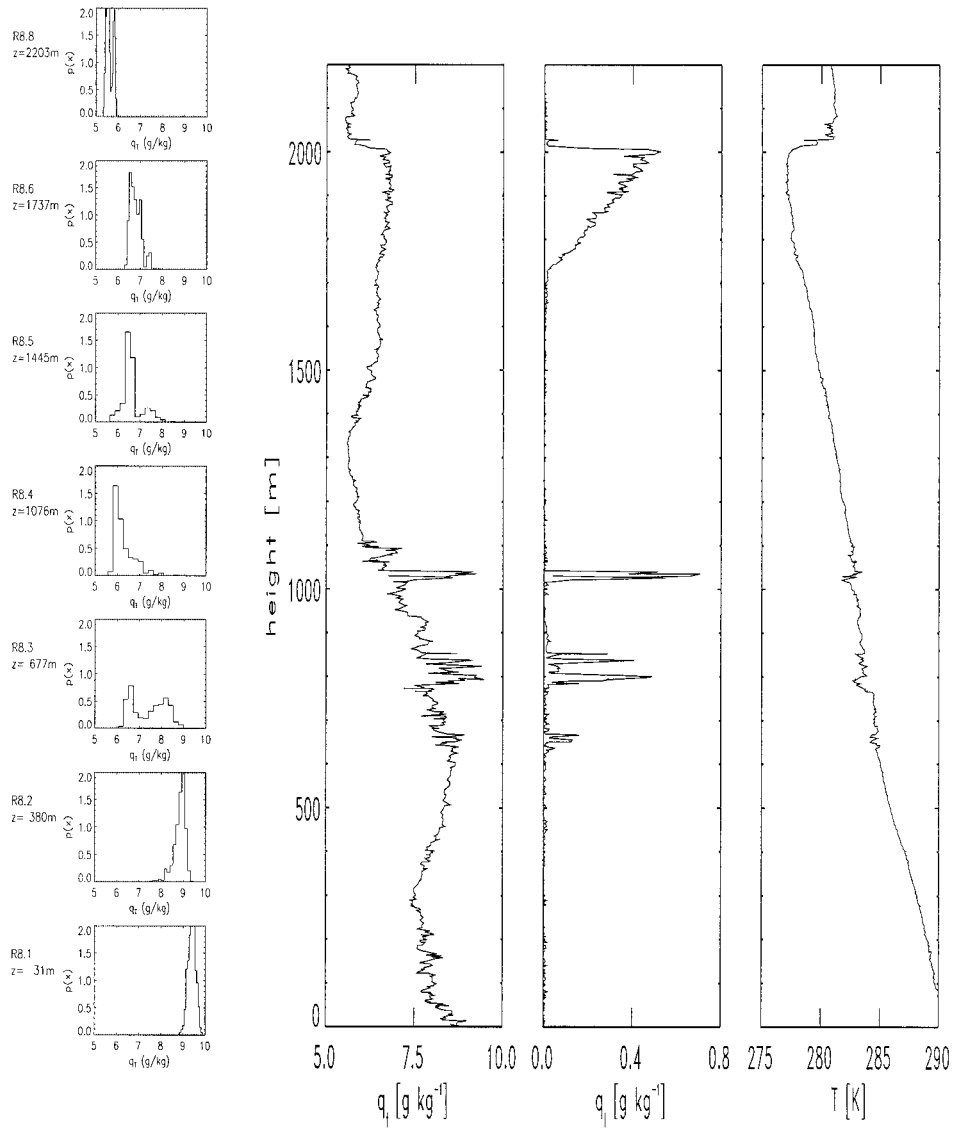

FIG. 2. Distributions of total water from a stack of seven horizontal runs through a decoupled boundary layer with stratocumulus and penetrative cumulus during ASTEX (flight A213), together with the total water, liquid water, and temperature profile.

relationship is henceforth referred to as FWI (Field and Wood I).

The variable $\overline{q_t}/\overline{q_{s(l,i)}}$ is not identically equal to the mean total water saturation ratio, which is denoted as $\overline{q_t/q_{s(l,i)}}$. The two, using Reynolds averaging, are related by

$$\frac{\overline{q_t}}{\overline{q_{s(l,i)}}} = \overline{\left(\frac{q_t}{q_{s(l,i)}}\right)} + \frac{\overline{q_t' q_{s(l,i)}'}}{\overline{q_{s(l,i)}^2}}. \tag{4}$$

Figure 4 shows a plot of $\overline{q_t}/\overline{q_{s(l,i)}}$ against $(\overline{q_t}/\overline{q_{s(l,i)}})$ for the EUCREX data, which shows that in almost all cases the run-mean relative humidity is almost equal to the normalized total water content $\overline{q_t}/\overline{q_{s(l,i)}}$ used in this analysis. The product term $\overline{q_t' q_{s(l,i)}'}/\overline{q_{s(l,i)}^2}$ is, for 87% of the runs, less than 5% of $\overline{q_t}/\overline{q_{s(l,i)}}$ (see histogram in inset of Fig. 4). The product term $\overline{q_t' q_{s(l,i)}'}/\overline{q_{s(l,i)}^2}$ for the EUCREX and FIRE data is generally even smaller than for the EUCREX data. Thus, it would make little difference to the form of the relationship in Fig. 3 if the run-mean relative humidity was used rather than $\overline{q_t}/\overline{q_{s(l,i)}}$ as the choice of independent variable, a fact that might prove useful in cloud schemes where relative humidity is the prognostic water vapor variable.

The relationship between the cloud fraction and the run-mean condensed water normalized with the run-mean saturation specific humidity is shown in Fig. 5 for all three experimental datasets. The data can all be described fairly well by a single relationship.

In an attempt to explain the relationship between cloud fraction and cloud condensate we assume a differential equation for the rate of change of cloud fraction

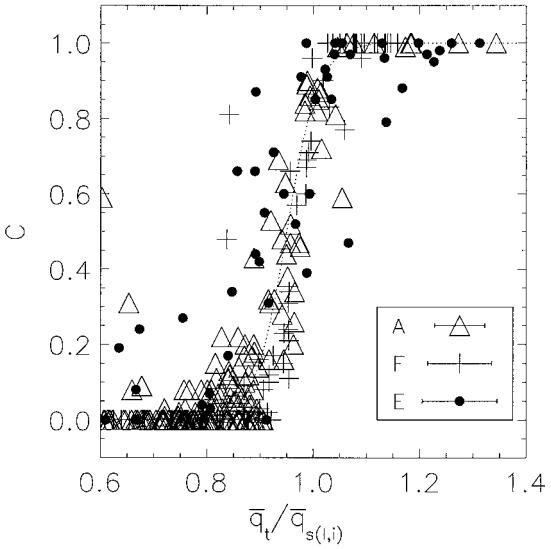

FIG. 3. Cloud fraction plotted against the run-mean total water content $\overline{q_t}$ normalized with the run-mean saturation specific humidity $\overline{q_{s(l,i)}}$. The approximate error in $\overline{q_t}/\overline{q_{s(l,i)}}$ is shown for each dataset in the inset. See text for more complete description of the errors. Datasets: FIRE (plus signs), ASTEX (triangles), and EUCREX (filled circles).

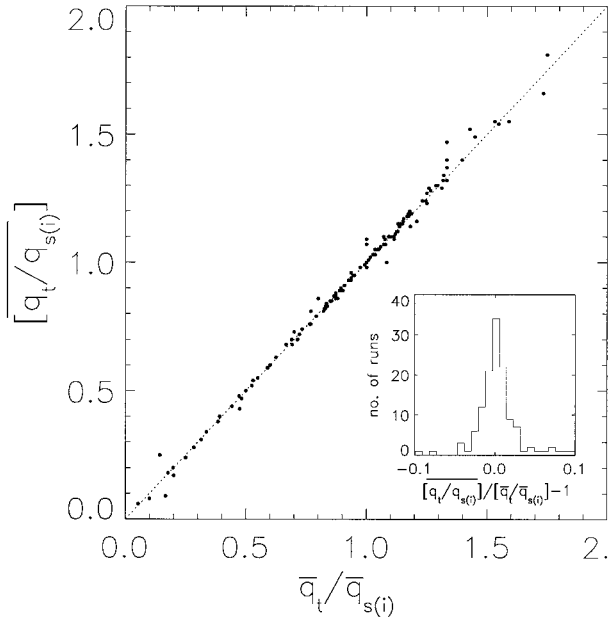

FIG. 4. Run-mean relative humidity, $(\overline{q_t}/\overline{q_{s(l,i)}}$, plotted against run-mean total water content $\overline{q_t}$ divided by the run-mean saturation specific humidity $q_{s(i)}$, for EUCREX data.

with respect to cloud condensate, $\partial C/\partial\overline{q_c}$. It is further assumed that the rate of change of cloud fraction is directly proportional to the fraction of clear sky remaining, that is,

$$\frac{\partial C}{\partial \overline{q_c}} = \frac{K(1 - C)}{\overline{q_s}}. \tag{5}$$

The saturation specific humidity is used as a normalization factor to nondimensionalize the constant K. The clear-sky fraction relation ensures that there is a smaller increase in cloud fraction for a small increase in $\overline{q_c}$ as the cloud fraction approaches 1 (addition of condensed water will tend to cause a larger increase in cloud fraction in a clear sky than an overcast one). Equation (5) can then be integrated with appropriate limits ($\overline{q_c} = 0$, $C = 0$) to obtain a relation for cloud fraction as a function of cloud condensate:

$$C = 1 - \exp(-K\overline{q_c}/\overline{q_s}). \tag{6}$$

From the best fit of (6) to the observational data of Fig. 5 a value of $K = 75.0$ was obtained. This functional relationship is denoted by the dotted line in Fig. 5 and is henceforth referred to as FWII (Field and Wood II).

4. Comparison of observations with parameterization schemes

The observational data in this study are used to validate cloud parameterization schemes that are either currently employed or could potentially be employed in large-scale climate and numerical weather prediction models. For this study we choose three schemes that were selected because of the differences in their conception: Slingo (1980), Smith (1990), and Xu and Randall (1996). Slingo (1980) uses GARP Atlantic Tropical Experiment (GATE) data to derive separate cloud parameterizations for low-, mid-, and high-level stratiform cloud. Smith (1990) does not quote as validation of his scheme experimental data of any kind but uses the assumption of subgrid distributions of humidity variables,

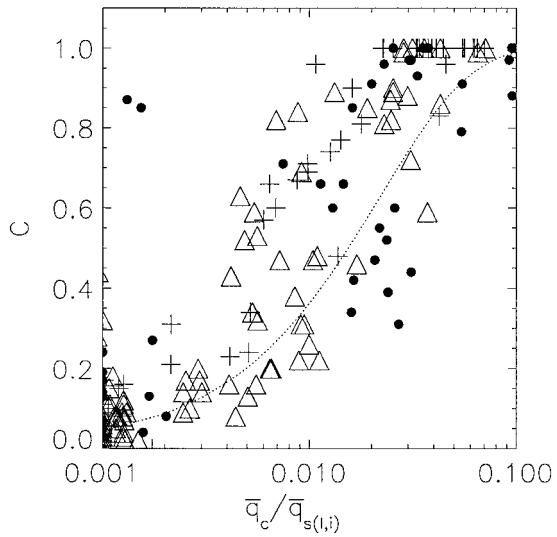

FIG. 5. Cloud fraction plotted against the run-mean condensed water content normalized by $\overline{q_{s(l,i)}}$. The approximate error in $\overline{q_c}/\overline{q_{s(l,i)}}$ is of the order of 15% for the ASTEX and FIRE cases and 20% for the EUCREX cases. Datasets: FIRE (plus signs), ASTEX (triangles), and EUCREX (filled circles).

TABLE 2. Summary of cloud parameterization schemes validated in this study.

Scheme	Physical basis	Outputs	Input parameter(s)
Slingo (1980)	GATE satellite and in situ observations	Cloud fraction	Relative humidity
Smith (1990)	Assumes form for subgrid distribution of total water	Cloud fraction and condensate	Relative humidity and critical-relative humidity
Xu and Randall (1996)	Cloud ensemble model	Cloud fraction	Cloud condensate, relative humidity, and saturation specific humidity

while Xu and Randall (1996) use results from multiple runs of a cloud ensemble model to derive relationships among cloud condensate, relative humidity (defined as $[\overline{q_t} - \overline{q_c}]/\overline{q_{s(l,i)}}$), and cloud fraction. Overviews of the three parameterization schemes are presented below, and Table 2 gives a brief summary of the features of the three schemes.

a. The Slingo scheme

The simplest of the three schemes is documented in Slingo (1980, henceforth SL80). Satellite observations of cloud fraction were obtained during GATE (Spackman 1975). Simultaneous thermodynamic observations were obtained from validated surface and upper-air observations from ships, land stations, and radiosondes. Low-level (warm) cloud was defined as that occurring below approximately 800 hPa, midlevel cloud as that occurring in the pressure range 400–800 hPa, and high (cold) cloud as that occurring about 400 hPa. Analysis of the GATE data culminated in three separate cloud fraction parameterizations for each of the three levels with each parameterization depending only upon the relative humidity. The SL80 scheme does not include a parameterization for the cloud condensate amount presumably, as this parameter was generally unavailable from GATE data.

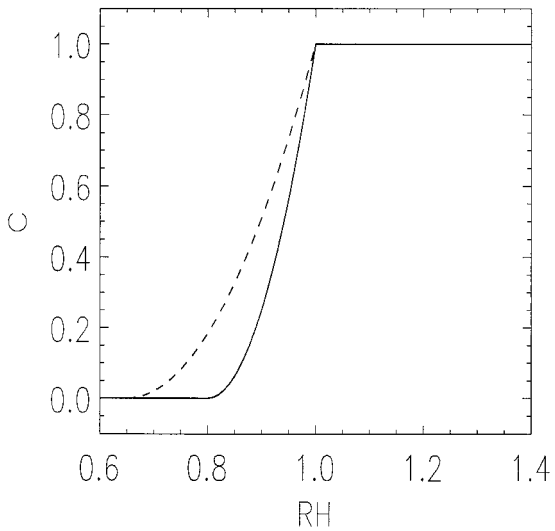

FIG. 6. Form of the diagnostic cloud fraction prediction scheme from Slingo (1980). Cloud fraction is plotted against relative humidity for high–low-level cloud (solid line) and midlevel cloud (dashed line). The definitions of the cloud types are given in the text.

The parameterizations for high-, mid-, and low-level clouds assume the form

$$C = \begin{cases} 0, & \text{RH} < M, \\ ([\text{RH} - M]/[1 - M])^2, & M \le \text{RH} < 1.0, \\ 1, & 1.0 \le \text{RH}, \end{cases} \tag{7}$$

where RH is the mean relative humidity. For low- and high-level cloud $M = 0.80$. For midlevel cloud $M = 0.65$.

Figure 6 shows the relationship between the cloud fraction and the normalized total water content for the SL80 scheme. The solid line is the relationship for low and high clouds and the dashed line is for midlevel cloud. For a grid box that is just saturated (RH = 1.0) the cloud fraction is unity.

b. The Smith scheme

The second scheme to be investigated is the diagnostic parameterization for cloud fraction and condensate used in the U.K. Meteorological Office (UKMO) Unified Model, first presented in Smith (1990, henceforth S90). Variants of the S90 scheme are used in several large-scale numerical models worldwide. The scheme assumes a symmetric triangular distribution for the subgrid variability in total water content (a prognostic variable) from which the cloud fraction and condensed water are derived. The use of distribution functions to account for subgrid variability follows the ideas of Sommeria and Deardorff (1977). The *critical-relative humidity* RH_{crit} is defined as the minimum grid-box mean relative humidity for which clouds will form and is essentially left as a free parameter to be specified. Values of RH_{crit} as a function of height have been derived by comparison of model output with data from Earth's Radiation Budget Experiment and ISCCP. The configuration that is currently employed in the UKMO Unified Model uses a critical relative humidity that is greatest (90%) close to the surface and that decreases with height in the boundary layer. Above the boundary layer a fixed constant value of the critical relative humidity is used (70%). We base our comparison upon the

scheme as it is implemented in the UKMO Hadley Centre climate model (Pope et al. 2000). In S90 the cloud fraction is a function of the total water content and $\mathrm{RH}_{\mathrm{crit}}$:

$$C = \begin{cases} 0, & \overline{q_t}/\overline{q_s} \le \mathrm{RH}_{\mathrm{crit}}, \\ \frac{1}{2}\left[1 + \frac{(\overline{q_t}/\overline{q_s} - 1)}{(1 - \mathrm{RH}_{\mathrm{crit}})}\right]^2, & \mathrm{RH}_{\mathrm{crit}} < \overline{q_t}/\overline{q_s} \le 1, \\ 1 - \frac{1}{2}\left[1 - \frac{(\overline{q_t}/\overline{q_s} - 1)}{(1 - \mathrm{RH}_{\mathrm{crit}})}\right]^2, & 1 < \overline{q_t}/\overline{q_s} < 2 - \mathrm{RH}_{\mathrm{crit}}, \\ 1, & 2 - \mathrm{RH}_{\mathrm{crit}} \le \overline{q_t}/\overline{q_s}. \end{cases} \tag{8}$$

The saturation specific humidity used is taken with respect to water for temperatures above 273.15 K and with respect to ice below this temperature. Figure 7a shows the relationship between $\overline{q_t}/\overline{q_s}$ and the cloud fraction from Eq. (8) for $\mathrm{RH}_{\mathrm{crit}} = 0.7$ (dashed), $\mathrm{RH}_{\mathrm{crit}} = 0.8$ (solid), and $\mathrm{RH}_{\mathrm{crit}} = 0.9$ (dotted). In each case the cloud fraction is zero for $\overline{q_t}/\overline{q_s} \le \mathrm{RH}_{\mathrm{crit}}$ and increases to reach 0.5 for $\overline{q_t}/\overline{q_s} = 1$.

c. The Xu and Randall scheme

Xu and Randall (1996, henceforth XR96) have developed a cloud parameterization scheme in a fundamentally different way from SL80 and S90. Instead of making assumptions about the subgrid variability of total water or similar parameter, XR96 have used repeated realizations from a cloud ensemble model to derive a relationship between cloud fraction, cloud condensate content, and relative humidity that can be used in a diagnostic sense in a large-scale model. Xu and Randall (1996) used the University of California, Los Angeles, cloud ensemble model with a three-phase bulk microphysical parameterization (Krueger et al. 1995) to simulate both boundary layer and tropospheric deep convective clouds. Unlike S90 the XR96 scheme does require additional means for prediction of the cloud condensate amount, and so the scheme is purely for use in predicting the cloud fraction.

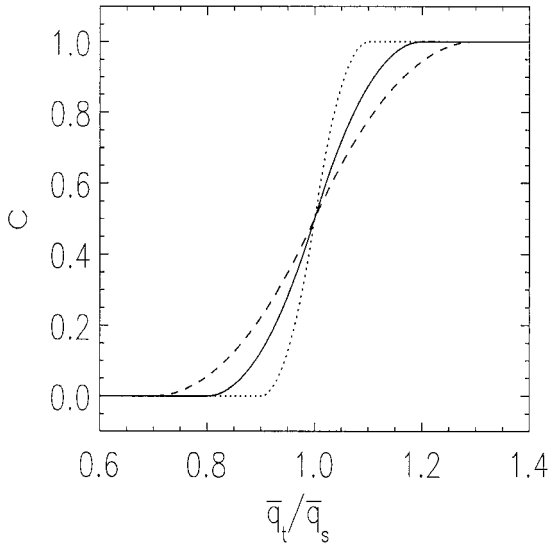

FIG. 7. Form of the diagnostic cloud fraction prediction scheme from Smith (1990). Cloud fraction is plotted against the run-mean total water content $\overline{q_t}$ normalized with the run-mean saturation specific humidity $\overline{q_{s(l,i)}}$. Curves for three values of $\mathrm{RH}_{\mathrm{crit}}$ are shown: dashed, $\mathrm{RH}_{\mathrm{crit}} = 0.7$; solid, $\mathrm{RH}_{\mathrm{crit}} = 0.8$; and dotted, $\mathrm{RH}_{\mathrm{crit}} = 0.9$.

The XR96 scheme, extended from initial work by Xu and Krueger (1991), is a modest breakthrough in the problem of predicting cloud fraction in large-scale numerical models for one major reason: the use of cloud ensemble models to determine relationships between cloud water and fraction provides a new and potentially fruitful avenue of research. Unlike S90 the XR96 scheme contains no free parameters and so comparison with observational data is relatively straightforward. The precise mathematical form of XR96 is given by

$$C = \begin{cases} (\mathrm{RH})^p[1 - \exp(-\alpha_0 \overline{q_c}/[(\overline{q_s} - \overline{q_v})]^\gamma)], & \mathrm{RH} < 1, \\ 1, & \mathrm{RH} \ge 1, \end{cases} \tag{9}$$

where $\overline{q_c}$ is the grid-box mean condensed water content, $\overline{q_s}$ is the saturation specific humidity, $p = 0.25$, and $\overline{q_v}$ is the water vapor content; $\alpha_0 = 100$ and $\gamma = 0.49$ are constants determined empirically from the cloud ensemble model data.

The functional relationships of the XR96 scheme are more difficult to depict graphically than for the S90 scheme as there is a dependence of the cloud fraction in XR96 on both the condensed water content and RH. The presence in Eq. (9) of the saturation specific humidity effectively introduces a height dependence into the cloud fraction parameterization since q_s decreases

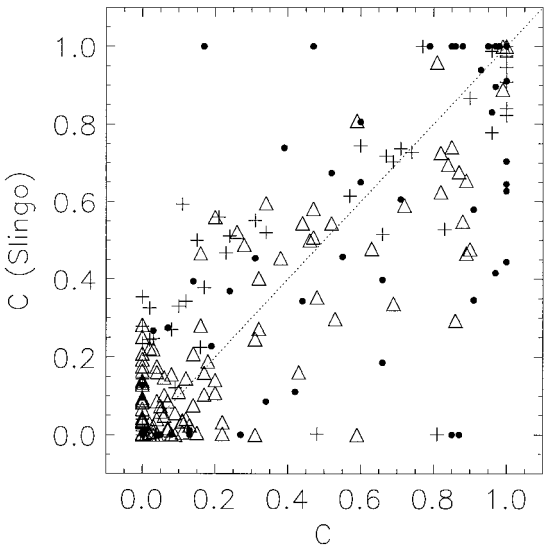

FIG. 8. Predicted cloud fraction using the Slingo (1980) scheme plotted against observed cloud fraction for FIRE (plus signs), ASTEX (triangles), and EUCREX (filled circles) data.

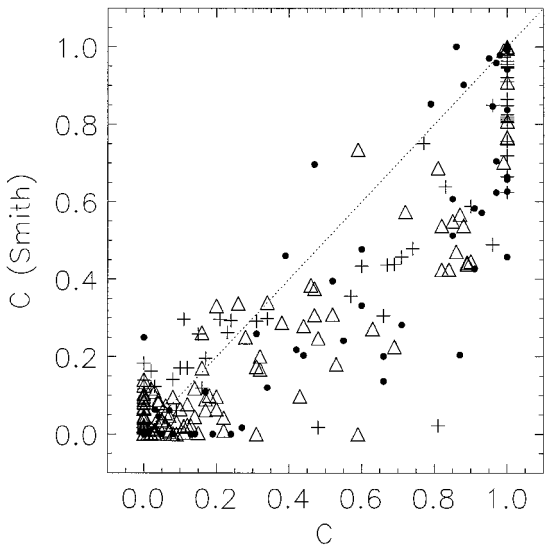

FIG. 9. Predicted cloud fraction using the Smith (1990) scheme plotted against observed cloud fraction for FIRE (plus signs), ASTEX (triangles), and EUCREX (filled circles) data.

with height (through its temperature dependence) almost everywhere in the troposphere.

A possible shortcoming with the XR96 scheme is that only two climatic conditions were simulated: tropical deep convection and mid-Atlantic high pressure boundary layers with strong subsidence inversions. The cold clouds in this study, for example, are predominantly forced by weak frontal uplift rather than strong convective motions. Different cloud water–cloud fraction relationships may exist for such markedly different physical systems.

d. Comparison with observational data

In this section measurements of cloud fraction, total water content, saturation specific humidity, and condensed water content are used to validate the three cloud fraction parameterization schemes described above. The two simple functional fits (FWI, FWII) to the data provided in this study are used as a reference in the comparison. Comparison of the C-130 cloud fraction observations with those parameterized in SL80, S90, XR96, and the simple fits FWI and FWII are shown in Figs. 8, 9, 10, 11, and 12 respectively. Obviously we have the advantage of fitting our relationships optimally to the data presented here and it would be possible to adjust the other schemes in the light of this data. For simplicity we chose to use the schemes in the form they were published. The different symbols represent data from the different experiments (as in Figs. 3 and 5) and the dotted line represents perfect agreement. Table 3 shows, for each experiment, parameterization scheme, and the two functional fits, the rms error between the predictions and the observations for three different cloud fraction bands (0–0.3, 0.3–0.7, 0.7–1). Table 4 shows, for each experiment and each parameterization scheme, the mean difference between the parameterized cloud fraction and the observed cloud fraction for the same three different observed cloud fraction bands.

The bias of the predictions for the schemes is up to 0.25 and can change signs between datasets for the same scheme. Both the Slingo and the Xu and Randall schemes do well in comparison to the functional fits, FWI and FWII, while the Smith scheme displays a consistent underestimate of cloud fraction. The rms differences again indicate that the Xu and Randall scheme compares favorably with the reference fits, but for this

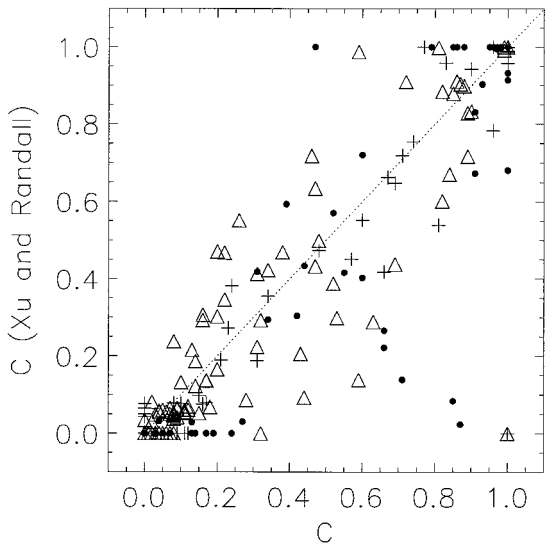

FIG. 10. Predicted cloud fraction using the Xu and Randall (1996) scheme plotted against observed cloud fraction for FIRE (plus signs), ASTEX (triangles), and EUCREX (filled circles) data.

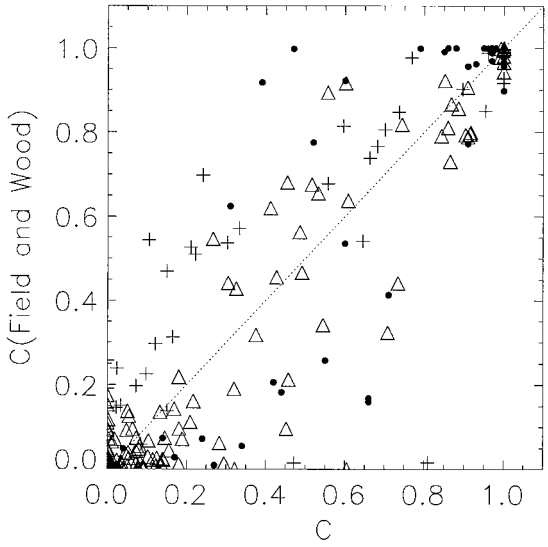

FIG. 11. Predicted cloud fraction using the functional fit, FWI, suggested in this paper plotted against observed cloud fraction for FIRE (plus signs), ASTEX (triangles), and EUCREX (filled circles) data.

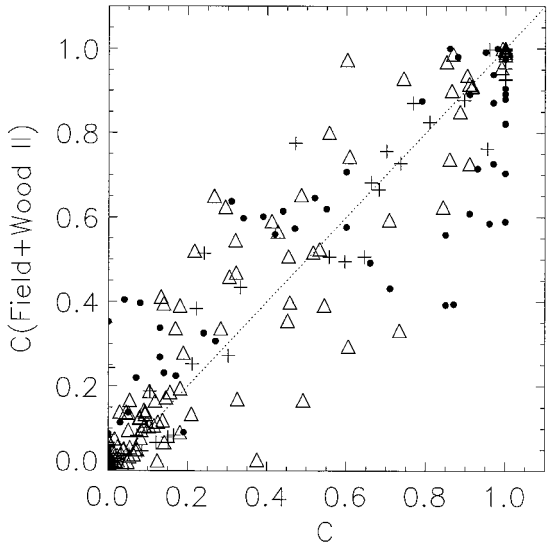

FIG. 12. Predicted cloud fraction using the functional fit, FWII, suggested in this paper plotted against observed cloud fraction for FIRE (plus signs), ASTEX (triangles), and EUCREX (filled circles) data.

aspect the Slingo scheme performs less well. Overall, the Xu and Randall scheme appears to have the least bias and spread, often outperforming the reference fits in the comparisons with the data.

5. Discussion and conclusions

While forecast models are tending to adopt dynamical schemes involving sources and sinks for the prediction of cloud fraction and condensed water content, observations presented here indicate that it is possible to diagnose cloud fraction from normalized total water content or a scaled cloud condensate content to a useful degree for stratocumulus cloud in the FIRE and ASTEX regions and midlevel ice cloud in the EUCREX region. A dynamical–microphysical prediction of cloud fraction is more satisfying in principle, but the increased number of tunable parameters makes this method less tractable until the physics of cloud formation and dissipation is known to a greater degree.

It is evident from Figs. 3 and 5 that cloud fraction is a sensitive function of the parameters used in this study. An important observation to note from Fig. 3 is that a cloud fraction of 1.0 is obtained for a $\overline{q_t}/\overline{q_{s(l,i)}}$ of approximately 1.05. This suggests that a symmetric unchanging probability distribution function of q_t (e.g., S90) is not applicable and the distribution is either strongly skewed (Bougeault 1981) or the formation of cloud forces the distribution to become modified (i.e., narrow). The authors plan to further investigate the distribution of atmospheric water along aircraft runs.

The existing cloud fraction parameterizations were tested in the form they were published. Even though it must be admitted that judicious choice of the tunable parameters associated with these schemes may have improved their performance in relation to the observations, it was found that the Xu and Randall scheme provided the greatest accuracy, comparing well with and even outperforming the reference fits.

It should be borne in mind that any parameterization of cloud fraction with variables such as $\overline{q_t}/\overline{q_{s(l,i)}}$ will not necessarily be applicable for climatic conditions that differ from those under which the observations were made. Therefore, until the physical reasons for such relationships are fully understood caution should be

TABLE 3. Comparison of cloud parameterization schemes with observational data. Root-mean-square error between predicted and observed cloud fractions for the three cloud fraction categories: 0–0.3, 0.3–0.7, 0.7–1.

	FIRE			ASTEX			EUCREX		
Parameterization	0–0.3	0.3–0.7	0.7–1	0–0.3	0.3–0.7	0.7–1	0–0.3	0.3–0.7	0.7–1
Slingo (1980)	0.27	0.21	0.18	0.11	0.22	0.21	0.29	0.28	0.35
Smith (1990)	0.09	0.26	0.26	0.07	0.27	0.28	0.14	0.27	0.30
Xu and Randall (1996)	0.07	0.11	0.21	0.09	0.24	0.23	0.14	0.25	0.28
Field and Wood I	0.22	0.20	0.16	0.10	0.24	0.08	0.14	0.34	0.19
Field and Wood II	0.07	0.19	0.12	0.10	0.22	0.15	0.13	0.33	0.24

TABLE 4. Comparison of cloud parameterization schemes with observational data. Mean difference between predicted cloud fraction and measured cloud fraction categorized by experiment for three measured cloud fraction categories: 0–0.3, 0.3–0.7, 0.7–1.

	FIRE			ASTEX			EUCREX		
Parameterization	0–0.3	00.3–0.7	0.7–1	0–0.3	0.3–0.7	0.7–1	0–0.3	0.3–0.7	0.7–1
Slingo (1980)	0.24	0.00	−0.06	0.00	−0.07	−0.13	0.08	0.00	−0.18
Smith (1990)	0.07	−0.22	−0.20	−0.04	−0.21	−0.23	−0.10	−0.18	−0.21
Xu and Randall (1996)	−0.03	−0.07	−0.04	0.00	−0.07	−0.05	−0.12	−0.03	−0.09
FWI*	0.19	0.03	−0.03	0.00	−0.04	−0.02	−0.12	−0.11	−0.05
FWII**	−0.04	−0.13	−0.08	0.02	−0.05	−0.06	−0.09	0.27	−0.09

* Field and Wood I
** Field and Wood II

used in regarding these results as both globally and temporally invariant.

Acknowledgments. The authors wish to thank the staff of Meteorological Research Flight, the C-130 RAF aircrew, and all of the other participants and organizers of the FIRE, ASTEX, and EUCREX projects. The authors also wish to thank Doug Johnson, Roy Kershaw, Steven Cusack, Gill Martin, Mark Webb, and Damian Wilson for providing valuable consultation and support.

APPENDIX A

Estimating Ice Water Content with the MRF Total Water Probe

We present a method of estimating ice water content in ice clouds that capitalizes on the unique instrument response of the Meteorological Research Flight (MRF) total water probe (Nicholls et al. 1990). Evidence is also provided that suggests that the method appears to be accurate to within 0.02 g kg^{-1}.

For this study the ice water content (IWC) was calculated using a total water probe mounted on the C-130. Brown and Francis (1995) detailed a method that found the IWC by subtracting a water vapor signal from the total water signal when the aircraft was known to be in ice cloud. The water vapor signal was provided by a Lyman-α fluorescence device that was also mounted on the C-130. In this appendix we suggest a very similar method to Brown and Francis, but obtain an estimate of the water vapor in cloud from the total water probe itself. The fluorescence device is in theory a self-calibrating device, but on a proportion of the high-level flights presented here, the calibration did not perform well and it is not thought to be accurate at pressures greater than 400 mb. Therefore, an alternative method was sought to obtain a measure of the water vapor in cloud.

The total water probe on the C-130 is a fast response instrument that measures the specific total water content (TWC) of a parcel of air. The data are recorded at 64 Hz, although the response has a slower response at low absolute total water contents. The method used by the probe is to rapidly convert all of the sampled water to vapor by means of efficient evaporators before measuring the total vapor density with a Lyman-α absorption hygrometer. The probe is not an absolute device and is calibrated against the General Eastern (GE) Dewpoint Hygrometer, which provides mass mixing ratios when operated in clear air.

The typical response of the total water probe in cold clouds is depicted in Fig. A1 (solid line). The spiked nature of the data is immediately obvious and is explained by realizing that as ice crystals enter the probe they are evaporated producing a very localized high value of water vapor density. The relatively low number concentrations of large ice particles means that individual arrivals are discernible. The total water probe time series thus consists of an environmental water vapor background with relatively discrete contributions from individual ice crystals. The assumption is made that the environmental water vapor background is the same as a minimum envelope fitted to the total water signal (dashed line in Fig. A1).

The method by which IWC is recovered from the total

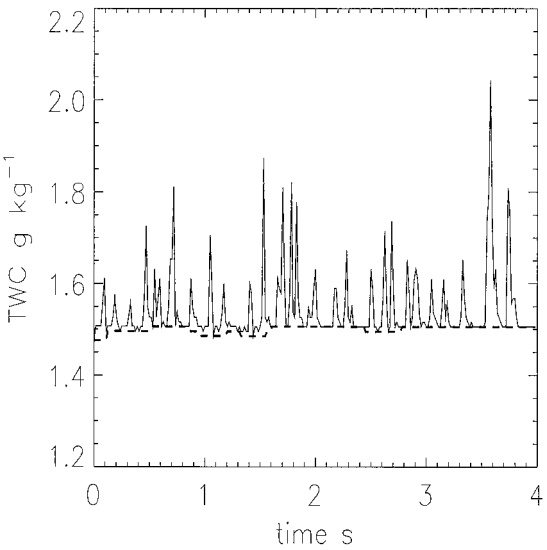

FIG. A1. Specific total water for 4 s obtained from the Meteorological Research Flight total water probe during a run in ice cloud (solid line). The minimum envelope fit to the data is shown as a dashed line.

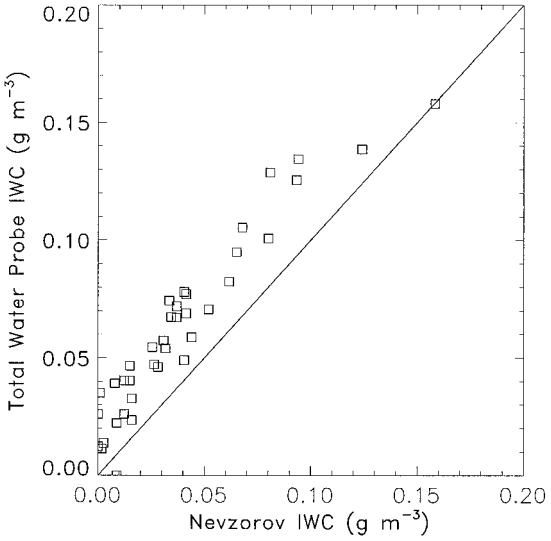

FIG. A2. Run-mean ice water content obtained from the Nevzorov probe plotted against the run-mean estimate of ice water content from the total water probe alone.

water content probe is as follows: first, fit a minimum envelope to the TWC time series using a window size of 10 Hz (which is longer than the length of a peak caused by individual ice particles) and then remove the minimum envelope from the 64-Hz TWC time series to leave just the ice particle signature. The remaining ice particle signature can then be averaged to provide a run-averaged IWC, for example.

A Nevzorov probe (Korolev et al. 1998) that measures total condensed water content was recently fitted to the C-130. An intercomparison was carried out for flight A661 (30 March 1999) between the Nevzorov probes estimate of IWC and the total water probe method of estimating the IWC to assess the acuracy of the total water probe method. Run averages (length 10 km) of IWC from the Nevzorov probe are plotted against the total water probe estimates in Fig. A2. The plot reveals that the total water probe estimate is 0.02 g kg^{-1} greater than the Nevzorov probe estimate. When this bias is removed the data have a random error of 0.02 g kg^{-1}. Therefore, the IWC for the EUCREX flights was estimated using the total water probe method outlined above with the subtraction of 0.02 g kg^{-1}.

APPENDIX B

Tabulated Observational Data

The aircraft run-mean observational data are presented in Fig. B1 in tabular form for each run from the three experiments (FIRE, ASTEX, and EUCREX). For each run the following information is given: Flt (Flight number), L (run length), T (air temperature), P (pressure), q_t (total water content), q_{liq} (liquid water content), q_{ice} (ice water content), and C (cloud fraction). The flight numbers for the different projects are H801–H813, FIRE; A203–A215, ASTEX; A279–A290, EUCREX.

Flight	L [km]	T [K]	P [hPa]	Qt [g/kg]	LWC [g/kg]	IWC [g/kg]	C
H801	66	281	895	7.6	0.25	0	1
H801	56	281.3	894	7.75	0.27	0	1
H801	56	281.7	903	7.72	0.17	0	1
H801	61	286.1	961	7.66	0	0	0
H801	57	286	961	8.09	0	0	0
H801	49	283	916	7.47	0	0	0
H801	56	282.8	917	7.29	0	0	0
H801	68	289.8	1010	8.52	0	0	0
H801	54	289.9	1009	8.62	0	0	0
H801	57	281.5	899	7.73	0.24	0	1
H801	54	282.3	898	6.6	0.14	0	0.81
H801	62	282	910	7.36	0.04	0	0.34
H801	58	282.2	910	7.46	0.05	0	0.66
H802	64	290.1	893	3.45	0	0	0
H802	59	290.1	893	3.55	0	0	0
H802	96	289.5	845	4.48	0	0	0
H802	63	281.7	917	7.99	0.44	0	1
H802	62	281.6	917	7.81	0.43	0	1
H802	59	282.3	931	8.22	0.19	0	1
H802	60	282.3	931	7.72	0.17	0	1
H802	63	283.8	952	7.89	0.01	0	0.15
H802	62	283.7	952	7.63	0	0	0.12
H802	61	289.5	894	4.01	0	0	0
H802	60	289.9	894	3.42	0	0	0
H802	63	288.1	1010	8.11	0	0	0
H802	58	288.3	1010	7.79	0	0	0
H802	58	285.8	979	7.61	0	0	0
H802	58	285.7	979	8.04	0	0	0
H802	60	282	916	7.54	0.31	0	0.83
H806	59	290.6	927	8.35	0	0	0
H806	61	290	923	7.14	0	0	0
H806	54	285.2	949	9.39	0.34	0	1
H806	52	284.5	942	9.09	0.37	0	1
H806	60	285.6	966	9.05	0.08	0	0.67
H806	72	285.9	966	9.31	0.1	0	0.96
H806	78	286.7	975	9.36	0.05	0	0.24
H806	63	286.8	982	9.13	0.01	0	0.17
H806	63	288.9	1009	9.3	0	0	0
H806	70	289.3	1009	9.41	0	0	0
H806	51	288.6	909	7.85	0	0	0
H806	66	289	909	7.65	0	0	0
H806	62	284.3	936	9.1	0.46	0	1
H806	74	284.5	936	9.28	0.53	0	1
H806	57	285.7	965	9.71	0.13	0	0.77
H806	65	285.6	965	9.09	0.09	0	0.71
H806	62	287.6	906	7.67	0	0	0
H806	72	288.6	903	7.72	0	0	0
H807	66	290.4	908	4.03	0	0	0
H807	61	287.1	924	7.17	0	0	0
H807	64	285	942	8.02	0	0	0
H807	65	286.4	959	8.14	0	0	0
H807	62	287.4	978	8.14	0	0	0
H807	66	288.6	995	8.75	0	0	0
H807	56	289.2	1007	9.36	0	0	0
H807	60	289.4	1007	8.84	0	0	0
H807	98	288.3	994	8.2	0	0	0
H807	61	285.2	959	8	0.01	0	0
H807	63	283.7	943	8.07	0.05	0	0.57
H807	60	284.2	920	7.3	0.12	0	0.48
H807	65	283	929	8.18	0.26	0	1
H807	64	291.9	891	4.81	0	0	0
H808	10	284.5	948	9.37	0.45	0	1
H808	25	284.6	948	9.32	0.46	0	1
H808	58	294.2	878	3.9	0	0	0
H808	51	294.3	872	4.01	0	0	0
H808	53	294.8	908	6.85	0	0	0
H808	175	294.4	871	3.24	0	0	0
H808	30	293.9	905	5.2	0	0	0
H808	30	286.2	974	9.15	0	0	0.11
H808	16	294.6	904	5.76	0	0	0
H808	173	294.4	870	3.87	0	0	0
H808	30	294.4	905	4.22	0.03	0	0
H808	30	289.4	1010	9.32	0	0	0
H809	63	292.9	919	4.6	0	0	0
H809	63	283.7	932	8.68	0.33	0	1
H809	57	286.9	984	8.93	0	0	0.03
H809	59	288.9	1010	9.12	0.01	0	0
H809	67	288.9	1011	9.24	0	0	0
H809	61	285.8	966	8.62	0.01	0	0.1
H809	58	284	934	8.87	0.32	0	1
H812	56	294.7	912	3.49	0	0	0
H812	62	283.3	933	8.76	0.53	0	1
H812	54	287.1	1001	9.04	0	0	0.02
H812	63	286	985	8.89	0.02	0	0.31
H812	62	293.8	915	3.48	0	0	0
H812	53	284.9	964	8.85	0.14	0	0.9
H812	65	284.2	948	8.86	0.28	0	1
H812	57	283.5	934	8.59	0.36	0	0.96
H812	61	286	984	8.91	0.02	0	0.21
H812	63	287.4	1007	9.22	0.01	0	0
H812	59	292.1	912	4.47	0	0	0
H813	56	281.2	916	6.87	0.03	0	0.23
H813	62	281.1	917	7.11	0.09	0	0.74
H813	62	282.7	936	7.09	0.01	0	0.16
H813	65	282.7	936	6.88	0	0	0.09
H813	58	288.9	1013	7.5	0	0	0
H813	65	289	1013	7.54	0	0	0
H813	61	285.6	970	7.32	0	0	0
H813	65	285.5	970	7.36	0	0	0
H813	56	282.7	936	7.11	0	0	0.02
H813	58	282.9	936	7.26	0.01	0	0.08
H813	61	281.3	917	7.18	0.05	0	0.6
H813	64	281	916	7.03	0.07	0	0.69
A203	60	282.6	929	6.66	0.01	0	0.12
A203	59	280.7	903	6.51	0.04	0	0.32
A203	30	279.3	887	6.49	0.16	0	0.82
A203	60	278.9	882	6.23	0.16	0	0.9
A203	78	284.2	932	5.78	0.01	0	0.08
A203	61	291.2	1026	7.73	0	0	0
A203	60	282.1	908	6.69	0	0	0.05
A203	60	280.5	884	6.38	0.03	0	0.43

FIG. B1.

Flight	L [km]	T [K]	P [hPa]	Qt [g/kg]	LWC [g/kg]	IWC [g/kg]	C
A203	61	280.5	856	4.46	0.04	0	0.59
A203	78	286.8	966	7.5	0	0	0.01
A203	60	284.1	915	6.4	0	0	0.03
A203	30	285.1	934	7.52	0	0	0.08
A203	30	283.3	906	6.7	0.01	0	0.08
A203	29	283.5	907	6.51	0.01	0	0.08
A203	31	282.8	897	6.2	0	0	0
A203	42	281.9	881	5.95	0	0	0.02
A203	42	289.1	987	8.22	0	0	0.01
A203	42	281.7	844	3.65	0	0	0
A203	41	289.3	994	8.22	0	0	0
A204	42	290.3	1025	8.17	0	0	0
A204	42	287.6	992	7.78	0	0	0
A204	42	284.7	957	7.53	0	0	0
A204	42	282	921	6.78	0	0	0.04
A204	42	280.4	903	6.66	0.05	0	0.47
A204	42	283.5	872	3.86	0	0	0
A204	42	289.2	1009	8.19	0	0	0
A204	42	287.8	992	8.19	0	0	0
A204	42	285	957	7.89	0	0	0
A204	42	282.5	921	7	0.02	0	0.17
A204	42	280.2	896	6.89	0.13	0	0.85
A204	41	283.6	872	3.91	0	0	0
A204	42	289.3	1009	8.23	0	0	0
A204	42	287.9	993	8.14	0	0	0
A204	41	284.9	955	7.72	0	0	0
A204	42	282.5	921	6.96	0.01	0	0.12
A204	42	280	892	6.72	0.09	0	0.89
A204	42	283.4	873	3.95	0	0	0
A204	41	289.3	1008	7.97	0	0	0
A204	43	288.1	993	7.94	0	0	0
A204	42	285.5	960	7.48	0	0	0
A204	42	282.8	925	6.84	0.01	0	0.09
A204	42	280.5	895	6.71	0.06	0	0.38
A204	42	282.2	875	4.59	0.02	0	0.09
A204	42	288.4	993	7.64	0	0	0
A204	42	285.5	959	7.54	0	0	0
A204	41	283	924	7.01	0.02	0	0.14
A204	41	280.8	894	6.63	0.04	0	0.16
A204	42	279	874	6.42	0.19	0	0.88
A204	41	288.7	994	7.59	0	0	0
A204	42	285.9	959	7.42	0	0	0
A204	42	283.2	924	6.88	0	0	0.03
A204	43	281.1	895	6.56	0	0	0
A205	61	290.5	1027	7.29	0	0	0
A205	61	286.8	981	7.08	0	0	0
A205	60	282.6	929	6.63	0.01	0	0.11
A205	60	281.3	911	6.48	0	0	0.06
A205	62	279.4	888	6.57	0.16	0	0.87
A205	59	278.9	882	6.22	0.16	0	0.89
A205	59	291.3	1026	7.67	0	0	0
A205	60	287.3	977	7.63	0	0	0
A205	67	284	936	7.09	0	0	0.07
A205	60	282.2	910	6.76	0.01	0	0.07
A205	59	281.5	899	6.6	0.02	0	0.1
A205	59	279	869	6.12	0.06	0	0.69
A205	60	292.1	1022	8.77	0	0	0
A205	59	287.4	965	8.48	0	0	0
A205	60	285.1	934	7.58	0.01	0	0.15
A205	59	283.4	907	6.55	0.01	0	0.08
A205	59	282.8	897	6.26	0	0	0
A205	59	281.9	884	6.4	0.01	0	0.04
A206	89	290.1	1010	10.56	0	0	0
A206	90	290.6	1010	10.7	0	0	0
A206	90	282.4	826	6.4	0	0	0
A206	90	281.7	826	7.47	0	0	0
A206	60	290.9	1024	10.77	0	0	0
A206	60	289.4	1000	10.26	0	0	0.03
A206	64	286.2	942	9.97	0.22	0	0.81
A206	63	284.8	872	7.83	0	0	0
A206	60	285.1	914	9.1	0.05	0	0.34
A206	60	291.6	1022	10.25	0	0	0
A207	51	277.7	874	5.92	0.18	0	0.72
A207	57	281.2	855	3.74	0.01	0	0.02
A207	50	278.9	890	5.83	0.06	0	0.31
A207	55	280	904	5.91	0.02	0	0.17
A207	52	283.1	942	6.24	0	0	0
A207	55	285.7	977	6.83	0	0	0
A207	54	289.6	1023	7.09	0	0	0
A207	57	289.4	1023	6.82	0	0	0
A207	53	289.4	1023	6.81	0	0	0
A207	51	289.5	1023	6.98	0	0	0
A207	55	281.2	839	3.66	0	0	0
A207	49	279	887	6.03	0.07	0	0.48
A207	55	280.6	908	5.97	0	0	0.06
A207	54	281.7	922	5.89	0	0	0.02
A207	57	284.4	957	6.49	0	0	0
A207	59	287.2	992	6.91	0	0	0
A207	62	289.8	1023	7.06	0	0	0
A207	61	279.1	869	4.31	0.06	0	0.31
A207	55	282	855	3.83	0	0	0
A207	56	279.6	887	5.64	0	0	0.02
A207	56	281.9	922	6	0	0	0
A207	57	284.5	956	6.66	0	0	0
A207	57	287.5	991	6.83	0	0	0
A207	59	290.1	1023	6.96	0	0	0
A208	60	291.2	1022	8.72	0	0	0
A208	53	287.2	972	8.64	0	0	0
A208	60	283.4	911	6.92	0	0	0
A208	60	281.8	877	6.02	0.01	0	0.03
A208	60	281.3	860	5.24	0	0	0
A208	60	283.3	829	3.46	0	0	0
A208	26	281.3	878	5.19	0.01	0	0.09
A208	31	282.6	831	3.53	0	0	0.01
A208	61	279.9	861	6.72	0.29	0	0.86
A208	57	280.4	873	7.33	0.2	0	0.99
A208	79	282.7	904	7.21	0	0	0.04
A208	77	284.8	940	7.6	0	0	0
A208	75	288.8	990	8.03	0	0	0
A208	63	291.4	1023	8.24	0	0	0
A208	75	282.6	808	3.08	0	0	0

FIG. B1 (*Continued*).

Flight	L [km]	T [K]	P [hPa]	Qt [g/kg]	LWC [g/kg]	IWC [g/kg]	C
A208	60	282.5	808	3.24	0	0	0
A208	59	280.2	868	6.58	0.04	0	0.53
A209	60	289	1009	10.05	0	0	0
A209	60	288.2	1000	10	0.01	0	0.28
A209	60	287.7	992	10.07	0.09	0	0.84
A209	60	286.9	976	10.2	0.34	0	1
A209	60	285.8	957	10.17	0.61	0	1
A209	60	288.5	936	9.01	0	0	0
A209	59	288.9	1008	9.93	0	0	0
A209	60	288	998	9.97	0.01	0	0.44
A209	60	287.5	992	9.97	0.07	0	0.82
A209	59	286.9	977	10.13	0.3	0	1
A209	60	285.7	957	10.1	0.56	0	0.99
A209	60	287.7	940	9.22	0.12	0	0.22
A209	59	288.4	936	9.03	0	0	0
A209	61	289	1007	9.8	0	0	0
A209	60	288.2	998	9.88	0	0	0.32
A209	59	287.7	992	9.86	0.05	0	0.52
A209	58	286.7	976	10.06	0.27	0	1
A210	59	293.2	1019	10.9	0	0	0
A210	98	292.8	1008	10.71	0	0	0
A210	59	289.9	968	9.98	0	0	0.02
A210	61	287.7	934	9.12	0.01	0	0.07
A210	53	285.6	900	8.91	0.03	0	0.14
A210	59	282.9	855	8.42	0.09	0	0.47
A210	62	283.2	841	7.44	0.08	0	0.22
A210	60	284.4	819	3.72	0	0	0
A210	63	284.8	823	3.76	0	0	0
A210	60	293.7	1019	10.63	0	0	0
A210	59	293	1008	10.56	0	0	0
A210	60	290.4	969	9.66	0	0	0
A210	59	288.5	935	8.78	0	0	0
A210	60	286.6	901	8.54	0	0	0
A210	59	287.3	857	4.57	0	0	0
A210	71	285.9	820	3.69	0	0	0
A210	11	293.4	1017	11.37	0	0	0
A211	60	291.7	1021	10.39	0	0	0
A211	60	288.9	981	9.8	0.01	0	0.06
A211	60	287.1	952	9.02	0.03	0	0.2
A211	63	285.8	925	9.23	0.04	0	0.16
A211	58	284.4	898	8.81	0.06	0	0.2
A211	59	284.4	836	7.53	0	0	0
A211	81	283.8	872	8.06	0.04	0	0.08
A211	60	292.7	1018	9.3	0	0	0
A211	64	289.7	982	9	0	0	0
A211	60	287.3	952	8.82	0	0	0
A211	60	285.3	927	7.97	0.01	0	0.11
A211	60	284.8	900	4.21	0	0	0.01
A213	61	289.3	1004	8.98	0	0	0
A213	90	289.3	1004	8.57	0	0	0
A213	90	284.7	946	7.94	0.01	0	0.18
A213	60	285.2	947	7.56	0	0	0.03
A213	60	282.7	903	6.38	0	0	0.02
A213	92	282	902	6.9	0.05	0	0.2
A213	90	278.9	850	6.8	0.24	0	0.59
A213	60	278.6	849	7.01	0.27	0	1
A213	70	277.8	834	7.28	0.59	0	1
A213	60	279.8	776	5.62	0	0	0
A213	59	290.7	1020	9.42	0	0	0
A213	61	287.4	979	8.89	0	0	0
A213	60	285.2	946	7.55	0.01	0	0.11
A213	59	282.3	902	6.39	0.01	0	0.08
A213	60	280	867	6.77	0.07	0	0.26
A213	60	277.3	821	6.86	0.41	0	1
A213	60	279.8	775	5.6	0	0	0
A213	60	288.1	988	8.05	0	0	0
A213	60	283.8	924	7.33	0.01	0	0.05
A213	61	277.3	820	7.39	0.71	0	1
A215	61	289.6	1004	7.83	0.01	0	0
A215	58	292	1016	8.57	0	0	0
A215	60	283.8	904	6.25	0	0	0
A215	59	278.2	836	6.14	0.03	0	0.63
A215	30	289.7	984	8.08	0.01	0	0
A215	27	279.8	847	6.16	0	0	0
A215	39	278.6	833	6.02	0.01	0	0.02
A215	60	291.5	1017	8.82	0	0	0
A215	60	286	949	8.34	0	0	0.04
A215	59	283.7	915	7.28	0.01	0	0.04
A215	60	282.1	890	6.68	0.04	0	0.13
A215	60	278.6	847	6.32	0.11	0	0.46
a279	78	246.4	411	0.66	0.006	0	0.19
a279	88	248.4	429	0.88	0.008	0.015	0.66
a279	82	250.5	448	1.13	0.011	0.043	1
a279	123	267.8	699	1.9	0.013	0.006	0.13
a279	90	261.3	574	2.62	0.112	0.004	0.85
a280	64	245.1	394	0.94	0.003	0.111	1
a280	75	249.5	426	1.25	0	0.095	0.97
a280	77	244.1	390	0.62	0	0.005	0.71
a280	64	249	426	0.89	0.001	0.031	0.44
a280	77	253.5	463	1.29	0	0.031	0.55
a280	63	242.3	378	0.71	0.001	0.055	1
a280	68	246.8	411	0.97	0	0.077	1
a281	55	245.5	467	0.72	0.003	0.014	0.47
a281	63	250	507	0.88	0.004	0.026	0.31
a281	55	256.4	573	1.3	0.009	0.003	0.27
a281	50	258.8	595	1.4	0.016	0	0
a281	48	254.1	550	1.26	0.028	0.023	0.42
a282	12	279	824	6.32	0.06	0	0
a282	59	262.8	573	1.97	0.044	0.006	0.08
a282	60	251.8	467	0.63	0.023	0	0
a282	56	246.5	430	0.61	0.012	0	0
a286	62	270.5	697	2.18	0.013	0	0.05
a286	64	265.8	596	4.34	0.024	0.544	1
a286	71	261	530	3.49	0.018	0.568	0.86
a286	57	255.4	468	1.92	0.008	0.157	0.88
a286	50	255.6	468	1.73	0.005	0.045	0.6
a286	64	248.4	411	1.05	0.018	0	0.17
a286	60	271.2	699	1.45	0.014	0	0
a287	71	261.1	618	2.04	0	0.028	0.6
a287	62	255.9	548	1.47	0.003	0.036	0.52
a287	60	251.7	504	1.11	0.004	0.027	0.39

FIG. B1 (*Continued*).

Flight	L [km]	T [K]	P [hPa]	Qt [g/kg]	LWC [g/kg]	IWC [g/kg]	C
a287	59	247.4	464	0.68	0.003	0	0.24
a287	61	256.4	551	1.09	0.002	0	0.13
a288	64	264.8	698	3.07	0.001	0.284	0.98
a288	60	259.4	621	1.65	0.002	0.021	0.66
a288	64	254	551	1.29	0.002	0.042	0.93
a288	59	249.6	507	0.96	0.003	0.015	0.85
a288	63	245.1	467	0.68	0.003	0.001	0.87
a288	56	254.4	551	1.54	0.004	0.182	0.95
a288	60	258.7	598	1.71	0	0.096	0.91
a288	59	252.2	530	0.96	0	0	0.14
a289	127	257.5	569	1.51	0.009	0.003	0.04
a289	72	257.9	574	1.59	0.033	0.03	0.34
a290	59	244.5	448	0.8	0.024	0.018	1
a290	60	244.5	448	0.79	0.015	0.016	0.96
a290	60	251.5	509	1.27	0.044	0.036	0.97
a290	60	251.5	509	1.23	0.03	0.024	0.91
a290	59	257.5	574	1.86	0.055	0.065	1
a290	59	257.6	575	1.83	0.041	0.065	1
a290	60	262.7	646	2.53	0.038	0.085	1
a290	61	262.6	647	2.48	0.03	0.074	0.97
a290	60	269.8	753	3.17	0.009	0	0.03
a290	64	269.8	753	3.18	0.01	0	0.07
a290	55	254.7	540	1.59	0.021	0.076	0.79

FIG. B1 (*Continued*).

REFERENCES

Albrecht, B. A., D. A. Randall, and S. Nicholls, 1988: Observations of marine stratocumulus clouds during FIRE. *Bull. Amer. Meteor. Soc.,* **69,** 618–626.

——, C. S. Bretherton, D. Johnson, W. H. Schubert, and A. S. Frisch, 1995: The Atlantic Stratocumulus Transition Experiment—ASTEX. *Bull. Amer. Meteor. Soc.,* **76,** 889–904.

André, J. C., and Coauthors, 1988: Evaporation over land surfaces: First results from HAPEX-MOBILHY special observing period. *Ann. Geophys.,* **5,** 477–492.

Atkinson, B. W., 1981: *Mesoscale Atmospheric Circulations.* Academic Press, 495 pp.

Bougeault, P., 1981: Modeling the trade-wind cumulus boundary layer. Part I: Testing the ensemble cloud relations against numerical data. *J. Atmos. Sci.,* **38,** 2414–2428.

Brown, P. R. A., and P. N. Francis, 1995: Improved measurements of the ice water content in cirrus using a total water probe. *J. Atmos. Oceanic Technol.,* **12,** 410–414.

de Roode, S. R., and P. G. Duynkerke, 1997: Observed Lagrangian transition of stratocumulus into cumulus during ASTEX: Mean state and turbulence structure. *J. Atmos. Sci.,* **54,** 2157–2173.

Ek, M., and L. Mahrt, 1991: A formulation for boundary-layer cloud cover. *Ann. Geophys.,* **9,** 716–724.

Gardiner, B. A., and J. Hallett, 1985: Degradation of in-cloud forward scattering spectrometer probe measurements in the presence of ice particles. *J. Atmos. Oceanic Technol.,* **2,** 171–180.

Harmer, J., C. G. Kilsby, S. R. Rudman, and J. H. Seymour, 1990: Temperature measurements on the C-130–working group report. MRF Internal Note 55. [Available from The Meteorological Research Flight, Y46 Building, DERA, Farnborough, Hampshire, GU14 0LX, United Kingdom.]

Korolev, A. V., J. W. Strapp, G. A. Isaac, and A. N. Nevzorov, 1998: The Nevzorov airborne hot-wire LWC–TWC probe: Principle of operation and performance characteristics. *J. Atmos. Oceanic Technol.,* **15,** 1495–1510.

Krueger, S. K., Q. Fu, K. N. Liou, and H.-N. Chin, 1995: Improvements of an ice-phase microphysics parameterization for use in numerical simulations of tropical convection. *J. Appl. Meteor.,* **34,** 281–287.

Le Treut, H., and Z.-X. Li, 1988: Using Meteosat data to validate a prognostic cloud generation scheme. *Atmos. Res.,* **21,** 273–292.

Martin, G. M., D. W. Johnson, D. P. Rogers, P. R. Jonas, P. Minnis, and D. A. Hegg, 1995: Observations of the interaction between cumulus clouds and warm stratocumulus clouds in the marine boundary layer during ASTEX. *J. Atmos. Sci.,* **52,** 2902–2922.

Mellor, G. L., 1977: The Gaussian cloud model relations. *J. Atmos. Sci.,* **34,** 356–358.

Minnis, P., P. W. Heck, D. F. Young, C. W. Fairall, and J. B. Snider, 1992: Stratocumulus cloud properties derived from simultaneous satellite and island-based instrumentation during FIRE. *J. Appl. Meteor.,* **31,** 317–339.

Moss, S. J., P. R. A. Brown, D. W. Johnson, D. R. Lauchlan, G. M. Martin, M. A. Pickering, and A. Spice, 1993: Cloud microphysics measurements on the MRF C-130: Working group report. MRF Tech. Note 12, Meteorological Research Flight, 147 pp. [Available from The Meteorological Research Flight, Y46 Building, DERA, Farnborough, Hampshire, GU14 0LX, United Kingdom.]

Nicholls, S., J. Leighton, and R. Barker, 1990: A new fast response instrument for measuring total water content from aircraft. *J. Atmos. Oceanic Technol.,* **7,** 706–718.

Ouldridge, M., 1982: An introduction and guide to the Johnson–Williams liquid water content meter. The Met. Office, 15 Internal Rep. 41, 15 pp. [Available from The Met. Office, London Road, Bracknell, Berkshire RG12 2SZ, United Kingdom.]

Pope, V. D., M. L. Gallani, P. R. Rowntree, and R. A. Stratton, 1998: The impact of new physical parametrizations in the Hadley Centre climate model—HadAM3. *Climate Dyn.,* **16,** 123–146.

Slingo, J. M., 1980: A cloud parameterization scheme derived from GATE data for use with a numerical model. *Quart. J. Roy. Meteor. Soc.,* **106,** 899–927.

Smith, R. N. B., 1990: A scheme for predicting layer clouds and their water content in a general circulation model. *Quart. J. Roy. Meteor. Soc.,* **116,** 435–460.

——, D. Gregory, and C. Wilson, 1990: Calculation of saturated specific humidity and large scale cloud. Unified Model Documentation Paper 29, 7 pp. [Available from The Met. Office, London Road, Bracknell, Berkshire RG12 2SZ, United Kingdom.]

Sommeria, G., 1976: Three dimensional simulation of turbulent processes in an undisturbed trade wind boundary layer. *J. Atmos. Sci.,* **33,** 216–241.

——, and J. W. Deardorff, 1977: Subgrid-scale condensation in models of nonprecipitating clouds. *J. Atmos. Sci.,* **34,** 344–355.

Stickney, T. M., M. W. Shedlov, and D. I. Thompson, 1994: Rosemount aerospace total temperature sensors tech. report, revision c. Tech. Rep. Rosemount Aerospace, Eagan, MN, 28 pp.

Sundqvist, H., E. Berge, and J. E. Kristjansson, 1989: Condensation and cloud parameterization studies with a mesoscale numerical weather prediction model. *Mon. Wea. Rev.,* **117,** 1641–1657.

Tiedke, M., 1993: Representation of clouds in large-scale models. *Mon. Wea. Rev.,* **121,** 3040–3061.

WMO, 1996: *Guide to Meteorological Instruments and Methods of Observation.* 6th ed. WMO-8, WMO.

Xu, K.-M., and S. K. Krueger, 1991: Evaluation of cloudiness parameterizations using a cumulus ensemble model. *Mon. Wea. Rev.,* **119,** 342–367.

——, and D. A. Randall, 1996: A semi-empirical cloudiness parameterization for use in climate models. *J. Atmos. Sci.,* **53,** 3084–3102.